SI Appendix*

Motile cilia of the male reproductive system require miR-34/miR-449 for development and function to generate luminal turbulence

Shuiqiao Yuan[1,2,a], Yue Liu[3,4,a], Hongying Peng[1,a], Chong Tang[1], Grant W. Hennig[1,5], Zhuqing Wang[1], Li Wang[3,4], Tian Yu[1], Rachel Klukovich[1], Ying Zhang[1], Huili Zheng[1], Chen Xu[3,4,b], Jingwen Wu[3,4,b], Rex A. Hess[6,b], Wei Yan[1,7,b]

[1]Department of Physiology and Cell Biology, University of Nevada, Reno School of Medicine, Reno, NV, 89557, USA
[2]Family Planning Research Institute, Center for Reproductive Medicine, Tongji Medical College, Huazhong University of Science and Technology, Wuhan, 430030, China
[3]Department of Histology, Embryology and Genetics, Shanghai Jiaotong University School of Medicine, Shanghai, 200025, China
[4]Shanghai Key Laboratory of Reproductive Medicine, Shanghai, 200025, China
[5]Department of Pharmacology, University of Vermont, Burlington, VT, 05405, USA
[6]Department of Comparative Biosciences, College of Veterinary Medicine, University of Illinois, Urbana, IL, 61802, USA
[7]Department of Obstetrics and Gynecology, University of Nevada, Reno School of Medicine, Reno, NV, 89557, USA

[a]: co-first authors
[b]: co-corresponding authors

*This file contains 6 supporting figures (Figs. S1-S6), one supporting table (Table S1) and legends for 11 supporting movies.

www.pnas.org/cgi/doi/10.1073/pnas.1817018116

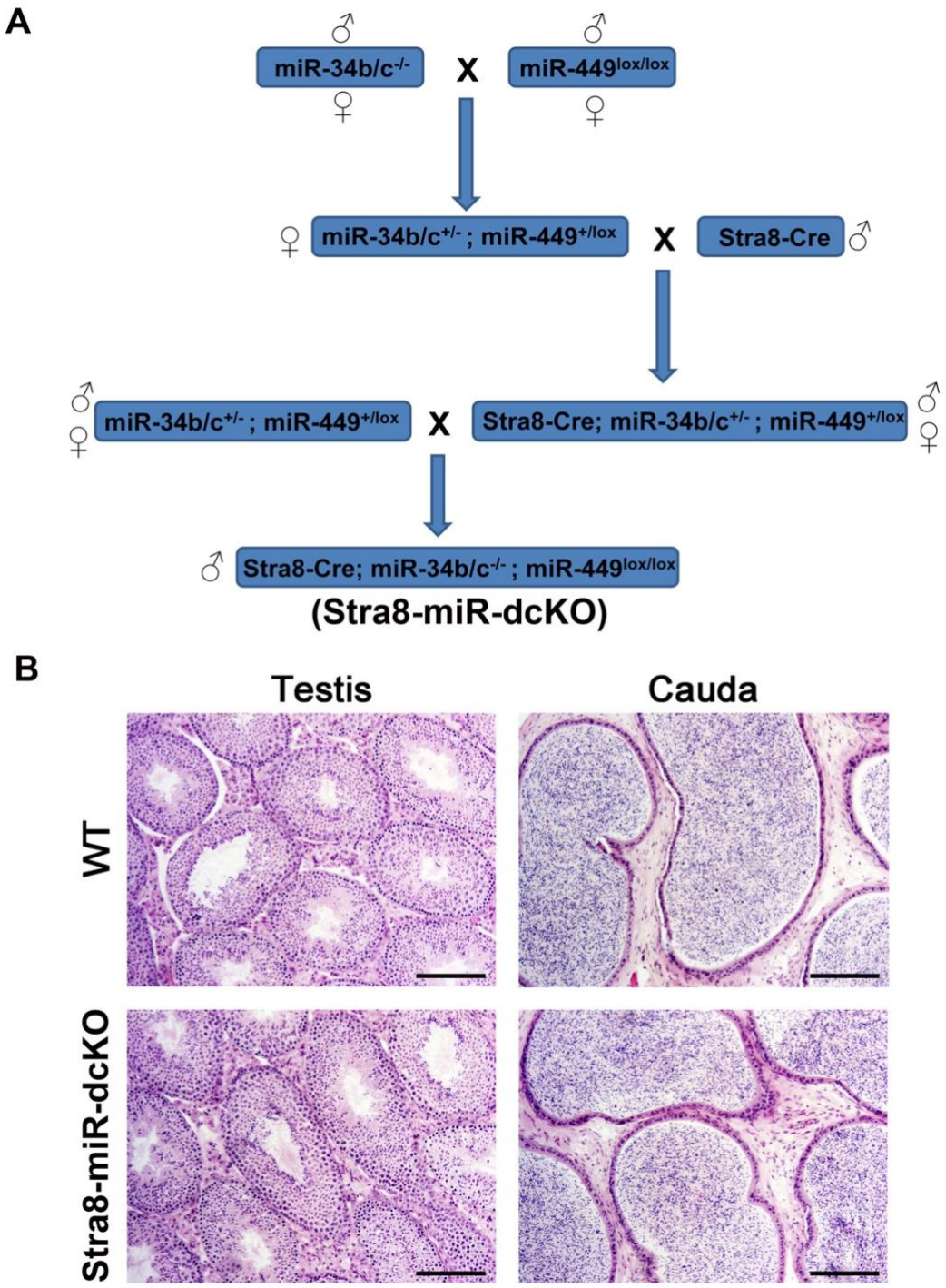

Figure S1. Spermatogenic cell-specific knockout of *miR-34b/c* and *miR-449* causes no spermatogenic disruptions in mice. (A) Breeding scheme used to generate spermatogenic cell-specific *miR-34b/c* and *miR-449* double conditional knockout (Stra8-miR-dcKO) mice (Stra8-Cre; *miR-34b/c*$^{-/-}$;*miR-449*$^{lox/-}$). (B) Histological analyses showing no spermatogenic defects in the Stra8-miR-dKO testis and cauda epididymis compared to WT controls. Scale bar=200μm.

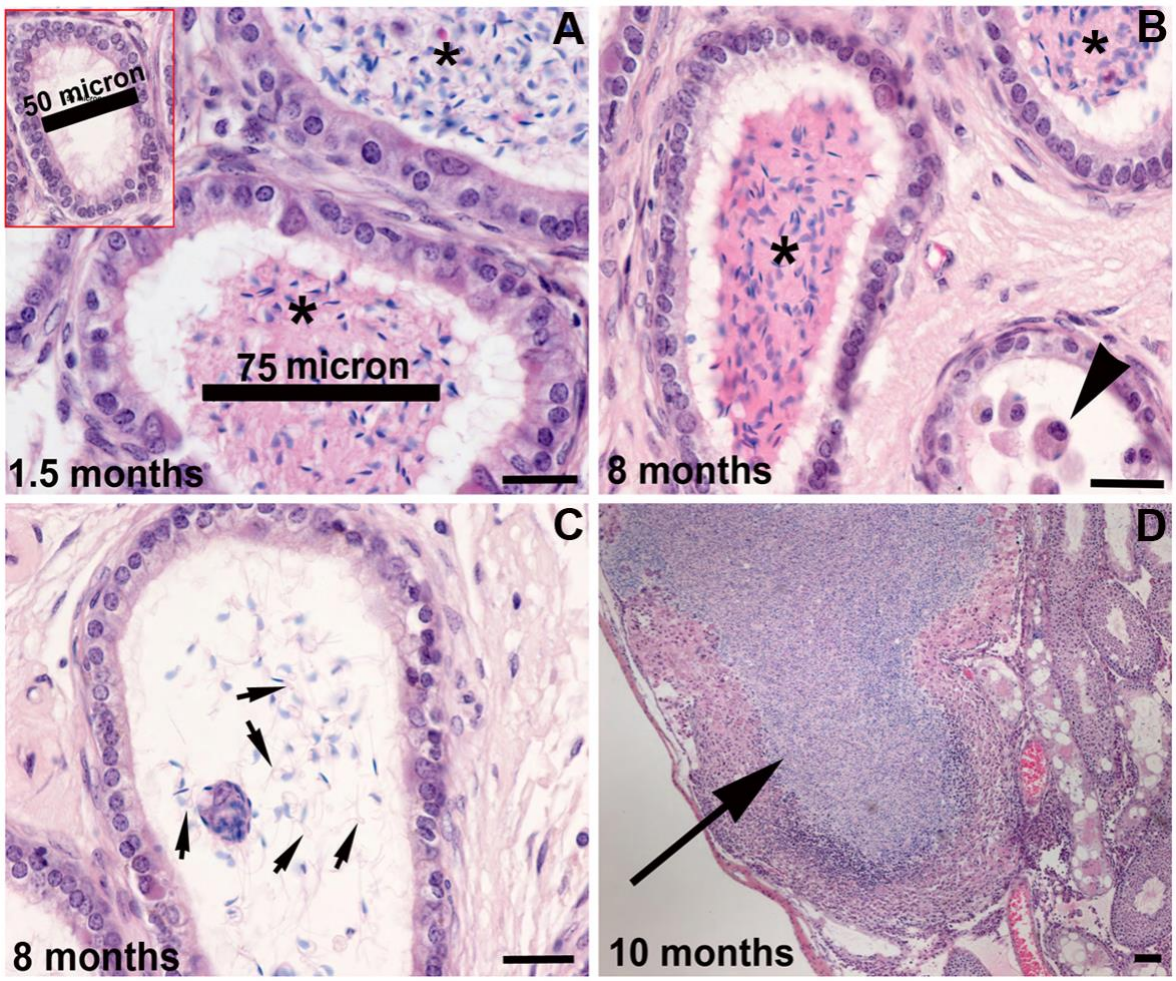

Figure S2. Sperm agglutination in the lumen of efferent ductules of miR-dKO male mice. (A) Large sperm agglutinations (asterisks) with a diameter larger than 75μm are present in the lumen of efferent ductules in a 1.5 month-old miR-dKO male mouse. Such a large sperm agglutination cannot pass the distal efferent ductules, which have a diameter of ~50μm (inset). (B) Large sperm agglutinations (asterisk) and numerous macrophages (arrowhead) are present in the lumen of efferent ductules of a 8 month-old miR-dKO male mouse. (C) Macrophages and sperm with highly coiled flagella in the lumen of efferent ductules of a 8 month-old miR-dKO male. (D) A large sperm granuloma (arrow) in the rete testis of a 10 month-old miR-dKO male mouse. Scale bar= 30μm.

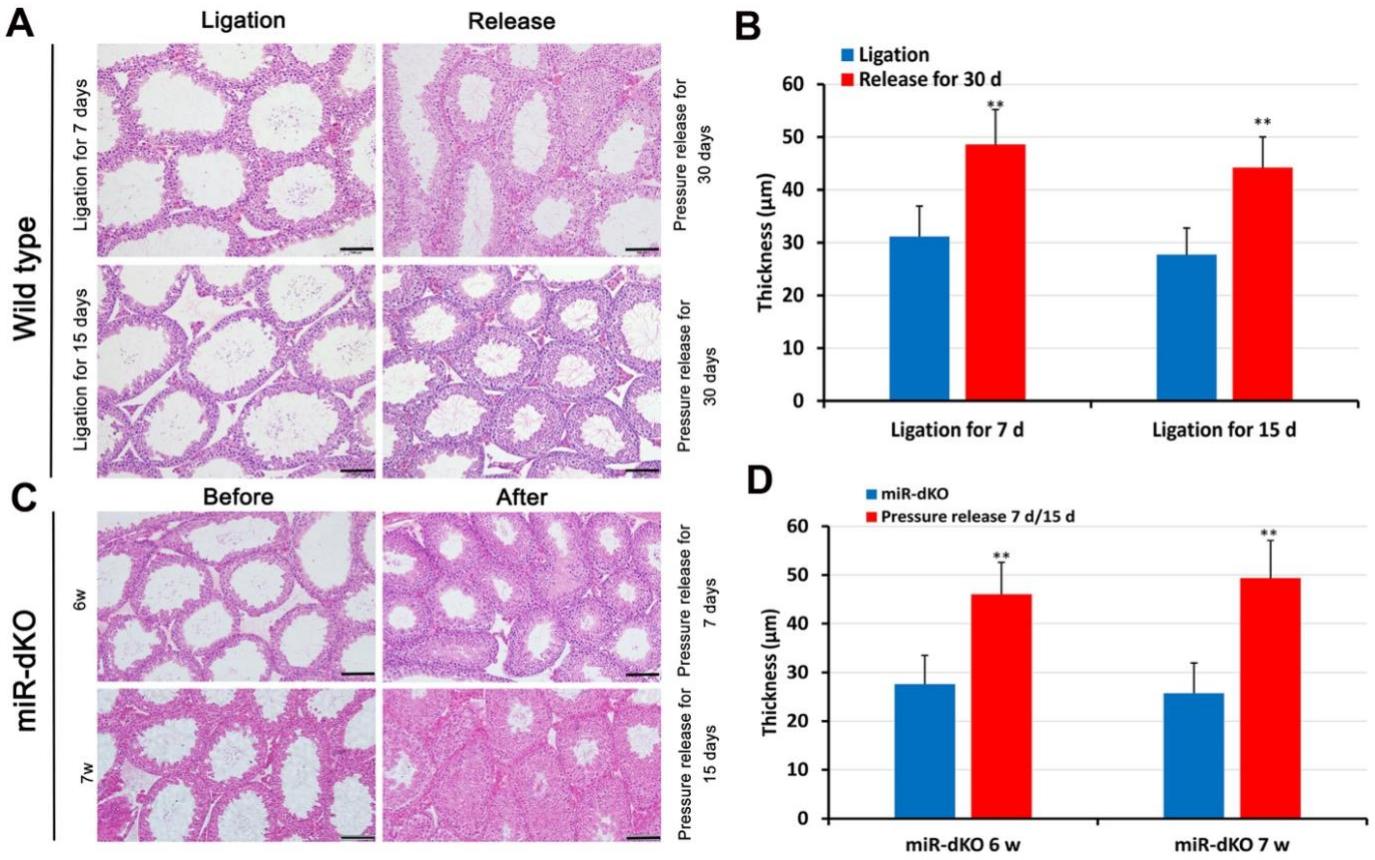

Figure S3. Ligation of the efferent ductules causes spermatogenic disruptions that are similar to those in miR-dKO, and pressure relief leads to recovery of spermatogenesis. (A) Testicular histology of adult wild type testes 7 and 15 days after ligation of efferent ductules using a surgical thread showing dilation of seminiferous tubules characterized by enlarged lumen and reduced stratification of the epithelium (left two panels). Fully recovered spermatogenesis 30 days after removal of the ligation thread (right two panels). (B) Quantitative analyses of the thickness of the seminiferous epithelium in adult wild type mice after ligation and removal of ligation thread. Data are presented as mean ± SEM (n=3). **: $p<0.01$ in student *t*-test. (C) Testicular histology of miR-dKO male mice at 6 and 7 weeks of age before and after release of back pressure by generating two tiny holes in the rete testis using a hooked surgical needle (diameter= 0.6mm). Scale bar= 200μm. (D) Quantitative analyses of the thickness of the seminiferous epithelium before and after surgical relief of the back pressure. Data are presented as mean ± SEM (n=3). **: $p<0.01$ in student *t*-test.

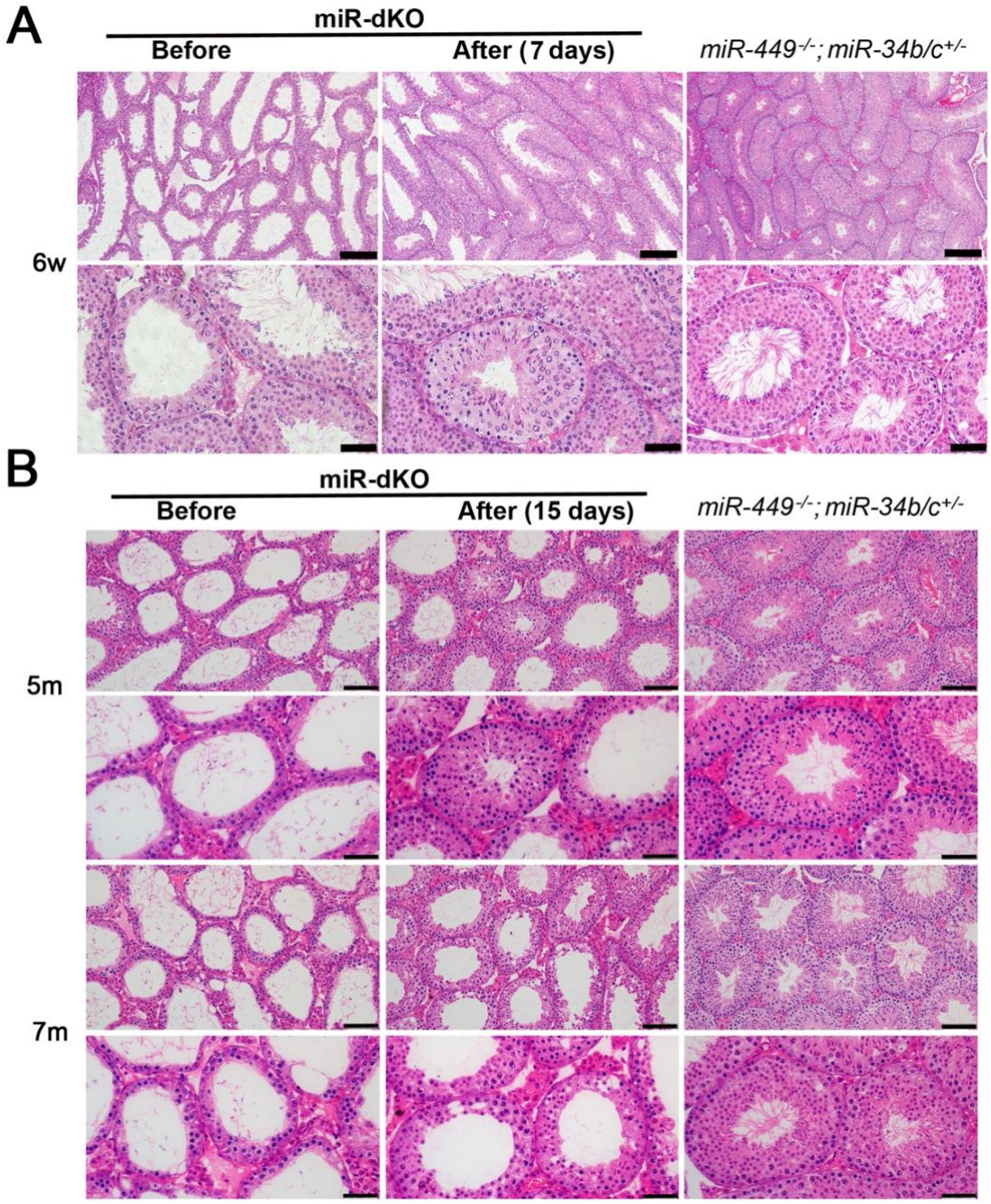

Figure S4. Recovery of spermatogenesis after pressure release in miR-dKO mice. (A) Low- (scale bar=200μm) and high-power (scale bar=50μm) testicular cross sections showing that spermatogenesis fully recovered 7 days after the surgical procedure in 6-week-old miR-dKO mice. (B) Low- (scale bar=100μm) and high-power (scale bar=50μm) testicular cross sections showing that spermatogenesis partially recovered 15 days after the surgical procedure in 5- and 7-month-old miR-dKO mice.

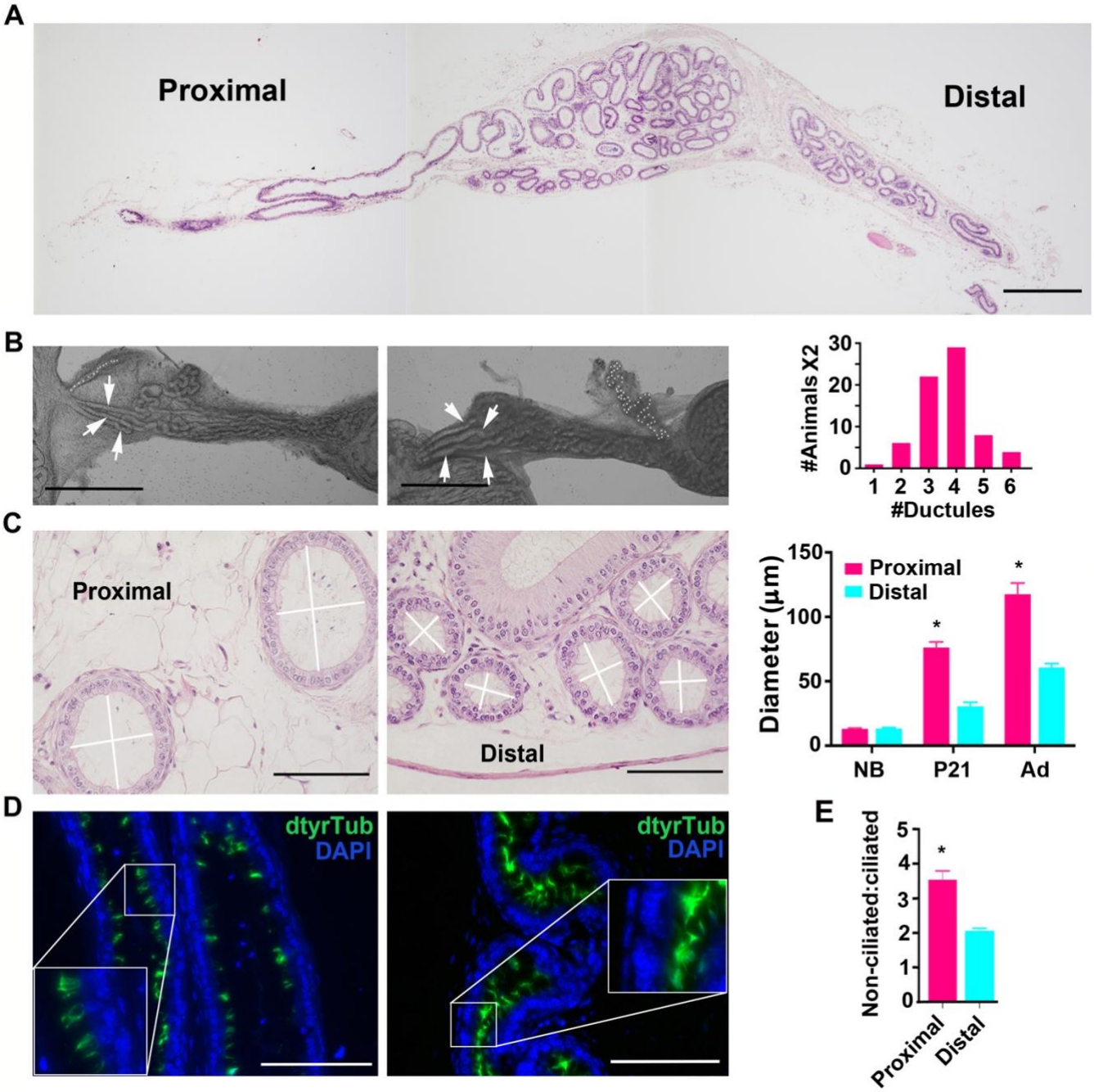

Figure S5. Histological analyses showing the structural features of the murine efferent ductules. (A) A HE-stained, longitudinal section of adult efferent ductules. Scale bar=500µm. (B) Representative mages of whole-mount newborn efferent ductules showing the most common number of efferent ductules tubules coming out of the rete testis (white arrows) is 3 or 4. A total 35 newborn mice (with efferent ductules connected to 70 testes) were studied. The white dotted lines indicated the blind-ended tubules. Scale bar= 2mm. (C) Representative HE-stained, close-to-round cross sections used for measuring the diameters of the proximal and distal segments of adult efferent ductules. Scale bar=100µm. Data are presented as mean ± SEM; n=6 for newborn (NB) and postnatal day 21 (P21) mice and n=12 for the adult group. *, statistically significant difference. (D) Representative immunofluorescent images showing more ciliated cells in the distal (right panel) than in the proximal (left panel) segments of the efferent ductules. Ciliated cells were detected using an antibody against detyrosinated α-tubulin (dtyr Tub), a marker for multiciliated cells, and the nuclei are counter-stained with DAPI (blue). Scale bar= 100 µm. (E) The ratio

of non-ciliated/ciliated cells in the proximal and distal segments of adult efferent ductules. Cell counting was performed on HE-stained paraffin sections. Data are presented as mean ± SEM; n=10. *, statistically significant difference.

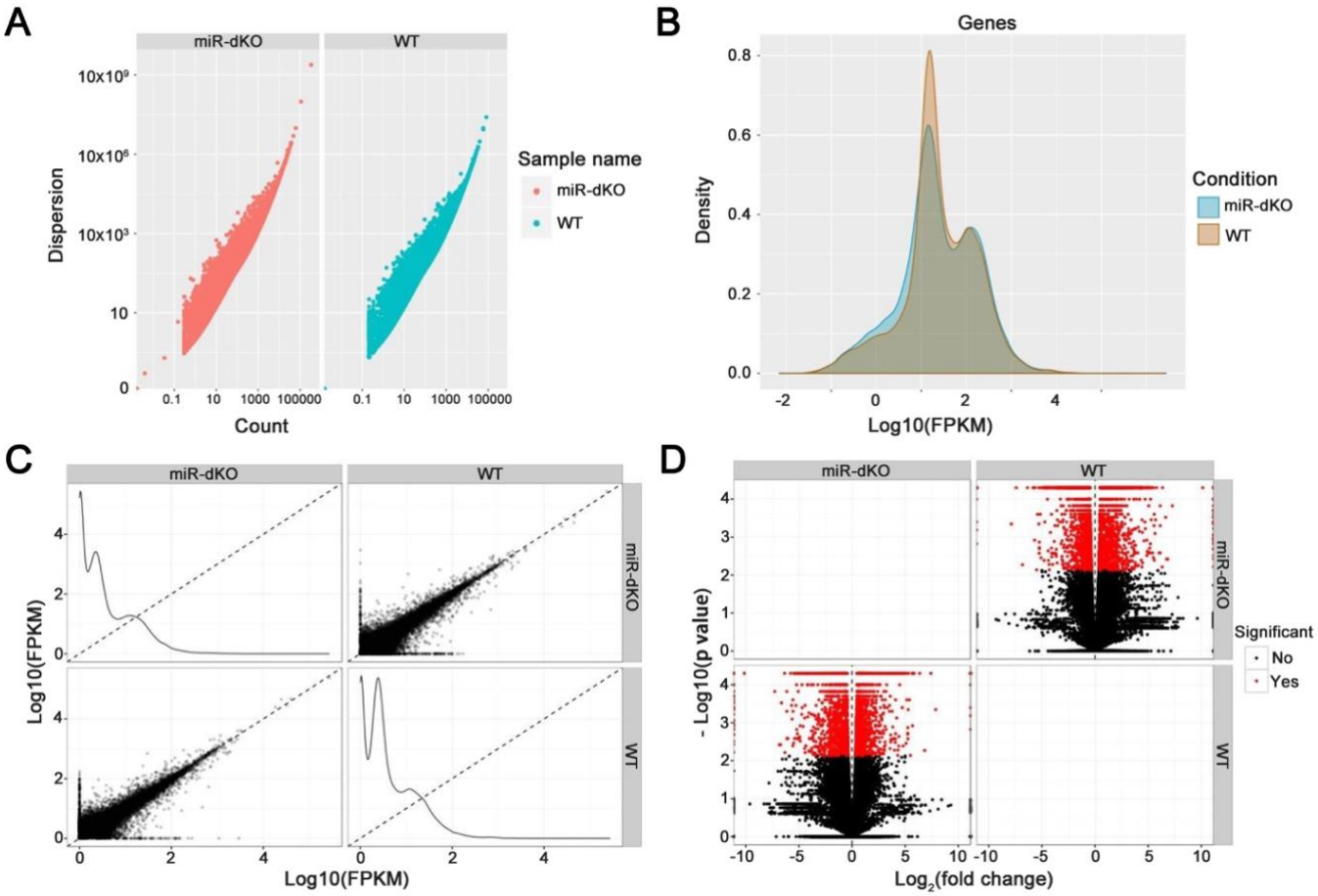

Figure S6. Evaluation of the quality of the RNA-Seq data generated in this study. (A) Over-dispersion plots demonstrating the estimated over-dispersion for each sample as a quality control measure. (B) Density plots showing the distribution of $\log_{10}$ normalized FPKM scores across biological replicates of two sample groups. (C) Scatterplot matrix showing the pairwise scatterplots of the $\log_{10}$ normalized FKMP scores across two sample groups. (D) The volcano plot showing the pairwise volcano plots of the $\log_2$ fold changes and associated $\log_{10}$ p-values across two sample groups.

SI Appendix: Table S1. Sequences of the primers used in this study.

Gene	Forward（5’ → 3’）	Reverse（5’ → 3’）
Cby1	AACAATCTCCTGCGGCTG	AACCTTCAGTTCATCCAGCTC
Ccdc113	TTCATCGGGCAATGGAGATC	CGTTCAAGATATGGGCTTTGG
Dnah6	GCCCAAGAAGCTGTGAAAAGG	CATGGAAGGTGTACGTCGGAT
Sclt1	CCAGGAGCTACTTTCTCAACTG	CGCCTTTGAAGTCTGTTTGC
Tubb4b	CTTCGGGCAGATCTTCAGAC	TCAGCTTCCTTTCTCACAACG
4931429I11Rik	CCGCCTCGAACAGATTTCCTA	CCTCTTGGGACATTGCCTGAT
Gapdh	AACTTTGGCATTGTGGAAGG	ACACATTGGGGGTAGGAACA
Ccdc113 3'UTR	CATCTCGAGTCAGGAGCAGCCGGCAGC	GATGCGGCCGCAACG GAAAATAATAGAGAA C
Dnah6 3'UTR	CATCTCGAGGTGGGAGCCTCGCCGATC	GATGCGGCCGCTTTCCAACAGAAATAACTCAAAACGAC

SI Appendix: Movie Legends

Movie S1. Cilia movement of a ciliated cell isolated from the EDs of a wild-type mouse causing propulsion and rotation.

Movie S2. Slow-motion movie clips showing cilial beating in a freely moving wild-type ciliated cell (left) and in the same ciliated cell with the cell body centered using motion stabilizing imaging routines (right). Scale bar=10μm.

Movie S3. Rapid cilial beating in an intact wild-type ED in which a standard deviation map of the fluctuation in grayscale intensity has been overlaid to highlight areas with greatest cilial movements (Fire LUT: small = purple, large = yellow/white). The cilia beating imparts a swirling motion to fluid and objects within the lumen of the ED.

Movie S4. Side view of cilial beating in an intact (whole mount) wild-type ED showing different frequencies and magnitudes of movement.

Movie S5. Top view of cilial beating in an intact (whole mount) wild-type ED showing spacing between tufts of cilia and their characteristics of movement.

Movie S6. Abnormal cilia length and movement of a ciliated cell isolated from the EDs of an adult miR-dKO mouse.

Movie S7. Another example of rigorous cilia beating and swirling motion of the luminal fluid and objects within an intact (whole mount) ED of a wild-type mouse.

Movie S8. Sparse, slow cilial beating in a whole mount ED of an adult miR-dKO mouse shows the loss of swirling motion of the luminal fluid.

Movie S9. Cilial beating causing fluid agitation and slow, multi-directional movement of spermatozoa in the proximal EDs of a wild-type mouse.

Movie S10. A shorter clip at a normal speed showing agitation of spermatozoa in the distal EDs of a wild-type mouse prior to the mass movement of spermatozoa in the lumen caused by a slow propagating contraction similar to peristalsis.

Movie S11. A longer clip at a faster playback speed showing peristaltic contractions of smooth muscle cause significant propulsion of spermatozoa within the lumen of distal EDs. Red and cyan colorings are thresholded differential objects (see methods) to better visualize movements.